

# Decoupled Dynamics Framework with Neural Fields for 3D Spatio-temporal Prediction of Vehicle Collisions

Sanghyuk Kim<sup>a</sup>, Minsik Seo<sup>b</sup>, Namwoo Kang<sup>b,c,\*</sup>

<sup>a</sup>Department of Mechanical Engineering, KAIST, Daejeon, 34141, Republic of Korea

<sup>b</sup>Narnia Labs, Daejeon, 34051, Republic of Korea

<sup>c</sup>Cho Chun Shik Graduate School of Mobility, KAIST, Daejeon, 34051, Republic of Korea

---

## Abstract

This study proposes a neural framework that predicts 3D vehicle collision dynamics by independently modeling global rigid-body motion and local structural deformation. Unlike approaches directly predicting absolute displacement, this method explicitly separates the vehicle's overall translation and rotation from its structural deformation. Two specialized networks form the core of the framework: a quaternion-based Rigid Net for rigid motion and a coordinate-based Deformation Net for local deformation. By independently handling fundamentally distinct physical phenomena, the proposed architecture achieves accurate predictions without requiring separate supervision for each component. The model, trained on only 10% of available simulation data, significantly outperforms baseline models, including single multi-layer perceptron (MLP) and deep operator networks (DeepONet), with prediction errors reduced by up to 83%. Extensive validation demonstrates strong generalization to collision conditions outside the training range, accurately predicting responses even under severe impacts involving extreme velocities and large impact angles. Furthermore, the framework successfully reconstructs high-resolution deformation details from low-resolution inputs without increased computational effort. Consequently, the proposed approach provides an effective, computationally efficient method for rapid and reliable assessment of vehicle safety across complex collision scenarios, substantially reducing the required simulation data and time while preserving prediction fidelity.

*Keywords:* Spatio-temporal prediction, Vehicle collision dynamics, Decoupled prediction framework, Coordinate-based neural networks, Physics-informed learning

---

## 1. Introduction

Vehicle collision safety remains a significant challenge in the automotive industry, with increasing demands for comprehensive safety validation. Regulatory bodies such as the New Car Assessment Program (NCAP) continuously enhance safety standards by incorporating diverse and complex collision scenarios [1]. These scenarios encompass diverse configurations, including oblique impacts and varying overlap ratios, providing a more accurate representation of real-world accident conditions [2, 3]. To ensure compliance with these evolving standards, each

---

\*Corresponding author

design modification necessitates extensive validation via physical crash tests and computational simulations [4]. Physical crash tests offer the highest fidelity in impact assessment; however, their high financial and resource demands hinder repeated design iterations. Meanwhile, full-vehicle simulations, while more feasible than physical tests, still require considerable computational power for multiple crash scenarios, posing a significant bottleneck in vehicle development cycles.

In vehicle collision dynamics, two key physical phenomena critically impact occupant safety: global rigid motion and local structural deformation. Global rigid motion, especially yaw motion around the vehicle’s vertical axis, determines the post-impact trajectory and may result in high-risk secondary impacts [5, 6, 7]. This motion significantly affects occupant kinematics and the overall crash safety performance. Equally important, local structural deformation governs how the vehicle’s structure absorbs and distributes impact energy, directly influencing occupant protection [8, 9, 10]. The interplay between these two phenomena directly dictates vehicle safety performance in real-world crashes. Modeling these coupled behaviors through finite element method (FEM) simulations [11] requires substantial computational resources because the calculations must simultaneously capture both large-scale rigid body dynamics and localized material deformations. This computational burden increases significantly when analyzing multiple crash scenarios with varied impact conditions, as required by current safety standards [1]. Thus, there is a clear need for more efficient prediction methods that can accurately model both global motion and local deformation while reducing computational demands.

To address computational challenges in collision dynamics, researchers have explored various deep learning approaches [12, 13, 14, 15, 16]. Convolutional neural networks (CNNs) handle regular grid-based problems but become impractical for high-resolution 3D predictions due to their memory scaling ( $O(N^3) \rightarrow O(N^4)$ ) [17]. Graph neural networks (GNNs), suited for structural meshes, struggle with long-range dependencies due to localized message passing [18, 19]. Recently, coordinate-based neural networks have gained attention for their memory-efficient, resolution-invariant modeling. These networks directly map spatio-temporal coordinates and simulation parameters to physical quantities without discretization, enabling efficient continuous prediction. Operator-learning frameworks, such as deep operator networks (DeepONet) [20], further extend this capability by mapping input functions to output fields. However, these methods model rigid motion and deformation jointly, introducing a trade-off between accuracy and efficiency. The inability to decouple these dynamics leads to unstable learning and degraded prediction performance in vehicle collisions. Long short-term memory (LSTM)-based models have been explored for spatio-temporal trajectory prediction [21, 22], but they assume rigid motion and fail to capture structural deformation, limiting their applicability to realistic crash scenarios.

The primary challenge in deep learning-based collision prediction arises due to the inherent complexity of vehicle collision dynamics. Global rigid motion and local structural deformation are governed by distinct physical principles and operate at different scales. Global motion involves complex rotational dynamics, which affect the entire vehicle structure, necessitating large receptive fields for accurate prediction. In contrast, local deformation requires high-resolution modeling of material responses in specific impact zones [23, 24]. Current deep learning approaches, regardless of their architecture, struggle to reconcile these trade-offs. Models optimized for global motion often lack the resolution for detailed deformation prediction, while those focused on local details fail to capture holistic vehicle dynamics [25, 26, 27, 28]. This fundamental trade-off between global and local behavior prediction represents a major challenge in designing practical deep learning solutions for vehicle collision analysis.

To address these fundamental challenges, we propose a novel deep learning framework that

decomposes vehicle collision dynamics prediction into specialized components. Rather than attempting to simultaneously capture both global and local behaviors in a single model, our architecture models rigid body motion and structural deformation within a latent space. This decoupled approach captures the distinct mathematical properties of each phenomenon, enhancing computational efficiency and prediction accuracy in practical vehicle safety assessments. Our main contributions are as follows:

- Develop a coordinate-based deep learning framework that decouples global rigid body motion from local structural deformation within a latent space without explicit supervision of either component.
- Implement a quaternion-based rotation representation that enforces  $SO(3)$  constraints, preventing gimbal lock and ensuring physically consistent vehicle trajectories under extreme impact conditions.
- Demonstrate that the proposed decoupled framework outperforms baseline models (Single MLP and DeepONet) in both interpolation and extrapolation, achieving up to 83.15% lower prediction errors while reducing training time by 83% through spatio-temporal sampling.
- Validate the framework’s resolution-invariant property, demonstrating its ability to infer high-resolution deformation fields from low-resolution training data, reducing reliance on costly high-resolution simulations.

The rest of this paper is structured as follows. Section 2 defines the collision prediction problem and presents our decoupled dynamics network, designed to separate global rigid motion from local deformation in the latent space. Section 3 describes the experimental setup, including simulation settings, baseline models such as a single multi-layer perceptron (MLP) and DeepONet, and hyperparameter configurations. Section 4 provides detailed experimental results, emphasizing the performance of the proposed framework in comparison to the baseline models. Finally, Section 5 discusses the broader implications of this study and delineates future directions for enhancing vehicle collision prediction and safety analysis.

## 2. Methodology

In this section, we introduce a novel decoupled prediction framework for accurately modeling 3D spatio-temporal vehicle collision dynamics. To overcome the limitations of traditional approaches, the proposed framework separately models global rigid-body motion and local structural deformation, enabling both higher accuracy and computational efficiency. The methodology comprises problem definition, the decoupled prediction framework, network architectures for global motion and local deformation, an integrated training procedure, and efficient spatio-temporal data sampling.

### 2.1. Problem definition

Accurately predicting vehicle collision dynamics necessitates the consideration of a diverse range of real-world collision scenarios. Vehicle collisions exhibit significant variability depending on factors such as impact speed, collision angle, overlap with obstacles, and impact distance. To effectively model and predict these scenarios, we define four key collision parameters that critically influence vehicle crashworthiness:

- **Initial velocity ( $v$ ):** The initial speed of the vehicle prior to impact, determining the kinetic energy involved and influencing impact severity.
- **Collision angle ( $\theta$ ):** The angle between the vehicle's trajectory and the barrier surface, influencing impact force distribution and deformation patterns.
- **Offset ratio ( $o$ ):** The overlap ratio between the vehicle front and the barrier, critically affecting impact area and structural integrity.
- **Distance ( $d$ ):** The initial distance between the vehicle and the barrier, defining the time to impact and influencing dynamic response characteristics.

These parameters span a range of impact scenarios, including high-severity collisions. Specifically, the collision angle  $\theta$  ranges from  $0^\circ$  to  $45^\circ$ , the velocity  $v$  ranges from 40 km/h to 80 km/h, the offset ratio  $o$  varies from 30% to 100% of the vehicle width, and the distance  $d$  ranges from 0.3 m to 2 m. This ensures broad model coverage, from low- to high-speed impacts and from head-on to oblique collision scenarios. An illustration of these collision conditions is shown in Figure 1.

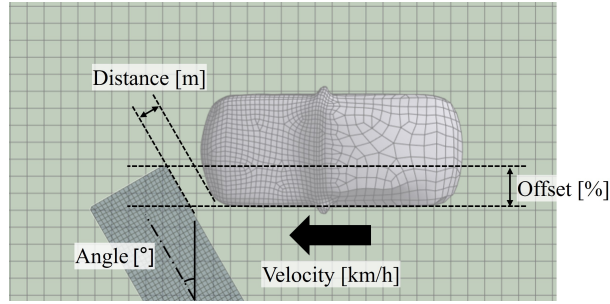


Figure 1: Initial collision conditions with key parameters: velocity ( $v$ ), collision angle ( $\theta$ ), offset ( $o$ ), and distance ( $d$ ).

## 2.2. Overview of decoupled prediction framework

To effectively model the complexities of vehicle collision dynamics, we propose a decoupled prediction framework that separates the prediction of global rigid-body motion from local structural deformation. The framework consists of two specialized neural networks: the *Rigid Net*, which predicts global rotation  $\mathbf{R}(t, \boldsymbol{\eta})$  and translation  $\mathbf{T}(t, \boldsymbol{\eta})$  based on collision conditions  $\boldsymbol{\eta} = [v, \theta, o, d]$  and time  $t$ , and the *Deformation Net*, which predicts local deformation displacement  $\mathbf{D}_i(t, \boldsymbol{\eta})$  for each node  $i$  considering its initial position  $\mathbf{x}_{\text{init},i} \in \mathbb{R}^3$ , the collision conditions  $\boldsymbol{\eta}$ , and time  $t$ . Unlike conventional approaches that directly estimate absolute displacements, our framework learns rigid body motion and deformation representations in a latent space, where each network implicitly captures distinct physical behaviors. This enables the model to generalize across diverse collision conditions without requiring explicit supervision for rigid and deformable motion components.

The predicted position of each node  $i$  at time  $t$ , denoted as  $\hat{\mathbf{x}}_i(t, \boldsymbol{\eta})$ , aims to satisfy the following condition:

$$\hat{\mathbf{x}}_i(t, \boldsymbol{\eta}) \approx \mathbf{x}_{\text{target},i}(t, \boldsymbol{\eta}), \quad (1)$$

where  $\mathbf{x}_{\text{target},i}(t, \boldsymbol{\eta})$  represents the ground truth position of node  $i$ . Accordingly, the predicted position is expressed as follows:

$$\hat{\mathbf{x}}_i(t, \boldsymbol{\eta}) = \mathbf{R}(t, \boldsymbol{\eta}) (\mathbf{x}_{\text{init},i} - \mathbf{c}) + \mathbf{c} + \mathbf{T}(t, \boldsymbol{\eta}) + \mathbf{D}_i(t, \boldsymbol{\eta}), \quad (2)$$

where  $\mathbf{R}(t, \boldsymbol{\eta}) \in SO(3)$  denotes the rotation matrix representing global rotation,  $\mathbf{T}(t, \boldsymbol{\eta}) \in \mathbb{R}^3$  denotes the translation vector representing global translation,  $\mathbf{D}_i(t, \boldsymbol{\eta}) \in \mathbb{R}^3$  represents the local deformation displacement of node  $i$ . The term  $\mathbf{c}$  denotes the centroid of the initial node positions. This decoupled approach enables each network to specialize in its respective task, leveraging distinct mathematical models from rigid body dynamics and structural deformation theory. Figure 2 illustrates the overall framework, showing how the two networks interact to produce the final positions of the nodes.

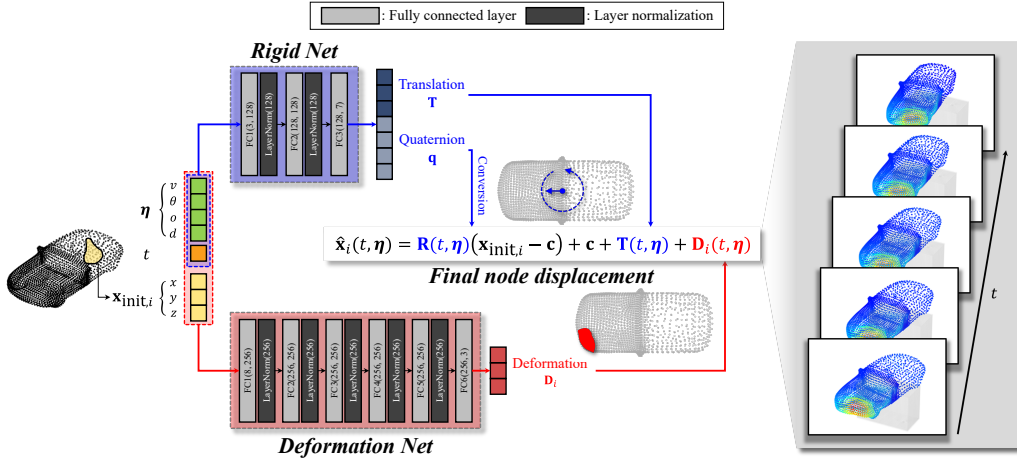


Figure 2: *Rigid Net* predicts 3D translation and quaternion-based rotation from time  $t$  and collision conditions  $\boldsymbol{\eta}$ . *Deformation Net* predicts 3D local deformation using  $t$ ,  $\boldsymbol{\eta}$ , and initial node position  $\mathbf{x}_{\text{init},i}$ . The final node displacement is obtained by summing rigid and deformation components. Both networks use ReLU activations.

### 2.3. Rigid Net: global rigid-body motion prediction

The *Rigid Net* predicts global rigid-body motion during collisions by modeling vehicle dynamics under the assumption that the vehicle behaves as a rigid body. The network estimates the vehicle's global rotation and translation, treating it as an idealized and undeformable rigid body. The network learns these predictions from collision conditions and time, without requiring explicit supervision for rotation or translation. Rather than directly predicting absolute motion parameters, the *Rigid Net* learns a latent representation of rigid body motion, where rotation and translation are implicitly inferred from collision conditions. This enhances generalization across diverse impact scenarios while ensuring physically consistent motion constraints.

The *Rigid Net* receives as input a 5-dimensional vector consisting of the four initial collision conditions ( $v, \theta, o, d$ ) and time  $t$ . The network outputs a 7-dimensional vector, where the first three elements represent the translation vector  $\mathbf{T} = [T_x, T_y, T_z]$ , and the remaining four elements represent the quaternion for rotational motion  $\mathbf{q} = [q_0, q_1, q_2, q_3]$ . The network consists of two hidden layers, each with 128 neurons, using ReLU activation functions and Layer Normalization after each hidden layer to improve training stability and convergence.

**Rigid-body rotation** Quaternions are employed to represent rotations, avoiding the limitations of gimbal lock by providing a rotation-invariant and continuous representation [29, 30, 31, 32]. A quaternion  $\mathbf{q}$  is defined as follows:

$$\mathbf{q} = q_0 + q_1\mathbf{i} + q_2\mathbf{j} + q_3\mathbf{k} = \cos \theta + (\sin \theta)\mathbf{I}(\mathbf{q}), \quad (3)$$

where  $q_0 = \cos \theta$  is the real part,  $\mathbf{I}(\mathbf{q}) = q_1\mathbf{i} + q_2\mathbf{j} + q_3\mathbf{k}$  is the imaginary part representing the axis of rotation. The quaternion encodes a rotation of  $2\theta$  around the axis  $\mathbf{I}(\mathbf{q})$ . To guarantee a valid rotation, we impose the unit-norm constraint on the predicted quaternion:

$$|\mathbf{q}| = \sqrt{q_0^2 + q_1^2 + q_2^2 + q_3^2} = 1. \quad (4)$$

This normalization enforces the unit-norm constraint required for valid rotations, ensuring that  $\mathbf{q}$  satisfies the fundamental trigonometric identity  $\cos^2 \theta + \sin^2 \theta = 1$ . By normalizing the quaternion directly, the network output remains stable and physically valid, which is critical for accurately modeling global vehicle motion during collisions.

**Rotation matrix conversion** The rotation matrix  $\mathbf{R}$  corresponding to the quaternion  $\mathbf{q}$  is derived as:

$$\mathbf{R} = \begin{bmatrix} 1 - 2(q_2^2 + q_3^2) & 2(q_1q_2 - q_3q_0) & 2(q_1q_3 + q_2q_0) \\ 2(q_1q_2 + q_3q_0) & 1 - 2(q_1^2 + q_3^2) & 2(q_2q_3 - q_1q_0) \\ 2(q_1q_3 - q_2q_0) & 2(q_2q_3 + q_1q_0) & 1 - 2(q_1^2 + q_2^2) \end{bmatrix}. \quad (5)$$

Since the rotation is applied around the centroid  $\mathbf{c}$ , we adjust the initial node positions accordingly:

$$\mathbf{x}_{\text{rotated},i}(t, \boldsymbol{\eta}) = \mathbf{R}(t, \boldsymbol{\eta})(\mathbf{x}_{\text{init},i} - \mathbf{c}) + \mathbf{c}. \quad (6)$$

This ensures a properly centered rotation, which is essential for accurate modeling of the vehicle's rotational motion.

**Rigid-body translation** The 3D translation vector  $\mathbf{T}(t, \boldsymbol{\eta})$  is applied to all nodes to account for the vehicle's translational movement:

$$\mathbf{x}_{\text{rigid},i}(t, \boldsymbol{\eta}) = \mathbf{x}_{\text{rotated},i}(t, \boldsymbol{\eta}) + \mathbf{T}(t, \boldsymbol{\eta}). \quad (7)$$

This finalizes the prediction of the vehicle's rigid body motion over time. Notably, the *Rigid Net* learns to predict translation and rotation parameters implicitly, as these outputs are not explicitly labeled during training.

#### 2.4. Deformation Net: local deformation prediction

The *Deformation Net* models the complex local deformations beyond the rigid body motion predicted by the *Rigid Net*. The network learns to predict the deformation displacement  $\mathbf{D}_i(t, \boldsymbol{\eta})$  as the residual between the true node position and the rigid body motion component  $\mathbf{x}_{\text{rigid},i}(t, \boldsymbol{\eta})$ . Thus, the *Deformation Net* captures fine-grained deformation patterns that complement global rigid-body motion. To achieve this, the network first learns a latent representation of deformation that captures spatial and temporal dependencies while explicitly disentangling it from rigid body motion. This enables the model to accurately capture fine-grained structural responses without explicitly separating deformation types.

The *Deformation Net* receives as input the initial position of each node  $\mathbf{x}_{\text{init},i}$ , time  $t$ , and the collision conditions  $\boldsymbol{\eta}$ . Thus, the input dimension is eight, comprising three for spatial position, one for the time step, and four for the collision conditions. The network outputs a 3-dimensional

vector  $\mathbf{D}_i(t, \boldsymbol{\eta})$ , representing the deformation displacement of node  $i$ . The network comprises four hidden layers, each containing 256 neurons. It employs ReLU activation functions and applies Layer Normalization after each layer to enhance training stability and convergence.

**Final node displacement** The total displacement of each node is defined as the sum of the deformation displacement predicted by the *Deformation Net* and the rigid body motion component:

$$\hat{\mathbf{x}}_i(t, \boldsymbol{\eta}) = \mathbf{x}_{\text{rigid},i}(t, \boldsymbol{\eta}) + \mathbf{D}_i(t, \boldsymbol{\eta}). \quad (8)$$

By incorporating both spatial and temporal information, the *Deformation Net* captures node-specific deformation patterns while ensuring physical consistency with the underlying material behavior. The network architecture is designed to capture complex nonlinear relationships inherent in both elastic and plastic deformations, thereby enabling accurate predictions across diverse collision scenarios.

### 2.5. Spatio-temporal data sampling

The proposed framework employs a coordinate-based neural network, which inherently exhibits resolution-invariant properties, enabling generalization across different spatial and temporal distributions. Leveraging this characteristic, we reduce computational cost by utilizing only 10% of the available data for training while maintaining predictive accuracy. The simulation dataset consists of 2,567 nodes evolving over 100 time steps, yielding a total of 256,700 node-time samples. Training on the entire dataset would impose a significant computational burden; therefore, we randomly sample 10% of the total data, selecting 25,670 node-time instances.

As shown in Table 1, using only 10% of the training data results in a test loss of  $5.41 \times 10^{-3}$ , which is comparable to the  $5.90 \times 10^{-3}$  obtained when training on the full dataset. Meanwhile, the total training time for 200 epochs with a batch size of 1,024 is significantly reduced from 208.32 minutes to 34.71 minutes, achieving an 83% reduction in computational cost. Notably, the resolution-invariant nature of coordinate-based neural networks enables the model to effectively predict the full spatio-temporal dynamics from a sparse subset of training samples. The effect of this sampling strategy is visualized in Figure 3, which illustrates the Euclidean distance error when performing inference on the non-sampled data from a specific test scenario after training with different sampling ratios. As the sampling ratio increases from 10% to 100%, the training loss decreases, while the test loss remains relatively stable. This indicates that the network possesses strong interpolation capabilities across spatial and temporal domains, allowing it to accurately capture vehicle collision dynamics even with a limited training subset. Consequently, the 10% sampling strategy achieves a favorable trade-off between computational efficiency and predictive performance.

Table 1: Training and test loss with various sampling ratios

Sampling ratio (%)	Train loss ( $\times 10^{-5}$ )	Test loss ( $\times 10^{-3}$ )	Total time (min)
10	1.25	5.41	34.71
20	0.76	5.91	54.19
40	0.52	6.64	93.98
80	0.38	6.73	167.19
100	0.34	5.90	208.32

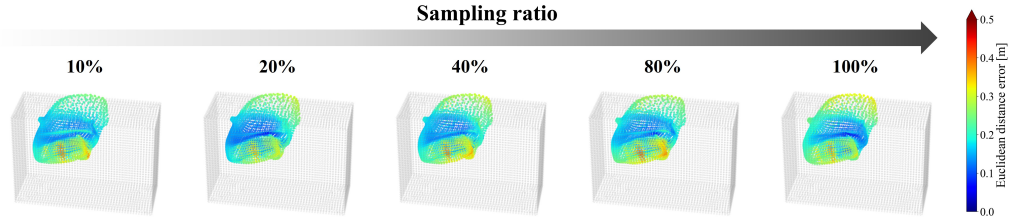


Figure 3: Model inference error across training dataset sampling ratios (10–100%).

### 2.6. Training procedure

Both the *Rigid Net* and *Deformation Net* are jointly optimized using a mean squared error (MSE) loss applied to node positions. For each node  $i$ , the optimization objective is to minimize the following loss function

$$\mathcal{L}_{\text{mse}} = \frac{1}{N} \sum_{i=1}^N \|\hat{\mathbf{x}}_i(t, \boldsymbol{\eta}) - \mathbf{x}_{\text{target},i}(t, \boldsymbol{\eta})\|^2. \quad (9)$$

Algorithm 1 details the training procedure, outlining the synchronized optimization of both networks. In each mini-batch, the *Rigid Net* outputs rotation quaternions (normalized to ensure valid rotations) and translation vectors, collectively defining the rigid-body displacement. Simultaneously, the *Deformation Net* refines node-level displacements by modeling local deformation patterns. These outputs are combined to produce the total predicted displacement for each node.

To ensure stable convergence, we employ the adaptive moment estimation (Adam) optimizer [33] for gradient updates, initializing it with a learning rate of  $1 \times 10^{-3}$ . A batch size of 1,024 is used to balance computational efficiency and gradient stability. The data loader ensures diverse coverage of collision conditions by shuffling and batching samples that include node positions, collision parameters ( $v$ ,  $\theta$ ,  $o$ ,  $d$ ), and time steps. This approach not only accelerates convergence but also maintains physically interpretable rigid motions and accurate local deformations across diverse crash scenarios.

---

**Algorithm 1** Training procedure for *Rigid Net* and *Deformation Net*

---

**Require:** Training dataset  $\mathcal{D}$ , where each node  $i$  has  $(\mathbf{x}_{\text{init},i}, \mathbf{x}_{\text{target},i}, \boldsymbol{\eta}_i, t_i)$ ; regularization weight  $\lambda$ ; maximum epochs  $E_{\text{max}}$ .

**Ensure:** Optimized parameters  $\omega_R$  (*Rigid Net*) and  $\omega_D$  (*Deformation Net*).

- 1: Compute global centroid:  $\mathbf{c} \leftarrow \text{mean}(\mathbf{x}_{\text{init},k} \in \mathcal{D})$ .
- 2: **for** epoch = 1 to  $E_{\text{max}}$  **do**
- 3:   **for** each batch of size  $N$  from  $\mathcal{D}$  **do**
- 4:     Extract  $(\mathbf{x}_{\text{init},i}, \mathbf{x}_{\text{target},i}, \boldsymbol{\eta}_i, t_i)$  for  $i = 1, \dots, N$ .
- 5:     Identify all unique pairs  $(t^\mu, \boldsymbol{\eta}^\mu)$  from  $\{(t_i, \boldsymbol{\eta}_i)\}_{i=1}^N$ .
- 6:     Define  $\pi(i)$  that maps node  $i$  to an index  $u$  corresponding to its unique pair  $(t^{\pi(i)}, \boldsymbol{\eta}^{\pi(i)})$ .
- 7:     **for** each unique pair  $(t^\mu, \boldsymbol{\eta}^\mu)$  **do**
- 8:        $(\mathbf{q}(t^\mu, \boldsymbol{\eta}^\mu), \mathbf{T}(t^\mu, \boldsymbol{\eta}^\mu)) \leftarrow \text{Rigid Net}(t^\mu, \boldsymbol{\eta}^\mu; \omega_R)$ .
- 9:        $\mathbf{q}(t^\mu, \boldsymbol{\eta}^\mu) \leftarrow \frac{\mathbf{q}(t^\mu, \boldsymbol{\eta}^\mu)}{\|\mathbf{q}(t^\mu, \boldsymbol{\eta}^\mu)\|}$ .
- 10:        $\mathbf{R}(t^\mu, \boldsymbol{\eta}^\mu) \leftarrow \text{QuaternionToMatrix}(\mathbf{q}(t^\mu, \boldsymbol{\eta}^\mu))$ .
- 11:     **end for**
- 12:     **for**  $i = 1$  to  $N$  **do**
- 13:        $\mathbf{x}_{\text{rigid},i} \leftarrow \mathbf{R}(t^{\pi(i)}, \boldsymbol{\eta}^{\pi(i)})(\mathbf{x}_{\text{init},i} - \mathbf{c}) + \mathbf{c} + \mathbf{T}(t^{\pi(i)}, \boldsymbol{\eta}^{\pi(i)})$ .
- 14:        $\mathbf{D}_i \leftarrow \text{Deformation Net}(\mathbf{x}_{\text{init},i}, t_i, \boldsymbol{\eta}_i; \omega_D)$ .
- 15:        $\hat{\mathbf{x}}_i \leftarrow \mathbf{x}_{\text{rigid},i} + \mathbf{D}_i$ .
- 16:     **end for**
- 17:      $\mathcal{L}_{\text{mse}} \leftarrow \frac{1}{N} \sum_{i=1}^N \|\hat{\mathbf{x}}_i - \mathbf{x}_{\text{target},i}\|^2$ .
- 18:     Update  $\omega_R, \omega_D$ .
- 19:   **end for**
- 20: **end for**
- 21: **return**  $\omega_R, \omega_D$

---

### 3. Experimental setup

This section presents the experimental setup, describing the simulation parameters, data generation process, and baseline models used for comparison. The simulation setup consists of a 3D vehicle model, material properties, and numerical configurations designed to replicate realistic crash scenarios. Data generation and processing procedure details the systematic sampling of collision conditions and the preprocessing strategies implemented to maintain dataset fidelity and diversity. Lastly, the baseline models, including coordinate-based neural networks (single MLP and DeepONet), are introduced with an emphasis on their architectures and training configurations, serving as a reference for evaluating the proposed framework.

#### 3.1. Simulation setup

The 3D vehicle model, derived from the ShapeNet dataset [34], is scaled to realistic automotive dimensions (Figure 4) to ensure that the simulated deformation patterns closely resemble real-world vehicle behavior. A shell-type finite element mesh is employed to balance computational efficiency and resolution, with a base element size of approximately 0.3 m and a refined frontal region to capture localized deformation. The shell thickness is set to 3 mm, reflecting typical automotive sheet metal. The final mesh, consisting of 2,567 nodes and 2,606 elements, provides sufficient resolution for modeling complex crash scenarios.

To replicate realistic crash scenarios, the vehicle structure is modeled using a generic aluminum alloy (Aluminum Alloy NL) with a density of  $2,770 \text{ kg/m}^3$  and a yield strength of 280 MPa. This material was chosen for its capability to represent the non-linear mechanical behavior of automotive-grade aluminum panels. Fatigue properties are referenced from MIL-HDBK-5H [35]. The barrier is modeled as a generic concrete material (CONC-35MPa) with a density of  $2,314 \text{ kg/m}^3$  and a compressive strength of 35 MPa [36, 37, 38]. This material is chosen to accurately capture energy absorption and damage patterns, ensuring reliable and stable simulation performance.

ANSYS Explicit Dynamics (AutoDyn) was employed to simulate high-strain-rate impacts across various collision conditions, including velocity, angle, offset, and distance. For the car-barrier interaction, a static friction coefficient of 0.8 and a kinetic friction coefficient of 0.7 were applied [39]. The barrier was fixed to the ground to prevent movement. The simulations consisted of 100 time steps with a step interval of 0.004 seconds, resulting in a total duration of 0.4 seconds. The minimum time step of  $1 \times 10^{-9}$  seconds and a safety factor of 0.9 were enforced to ensure numerical stability and accurately capture transient crash dynamics. Additional simulation parameters are provided in Table 2.

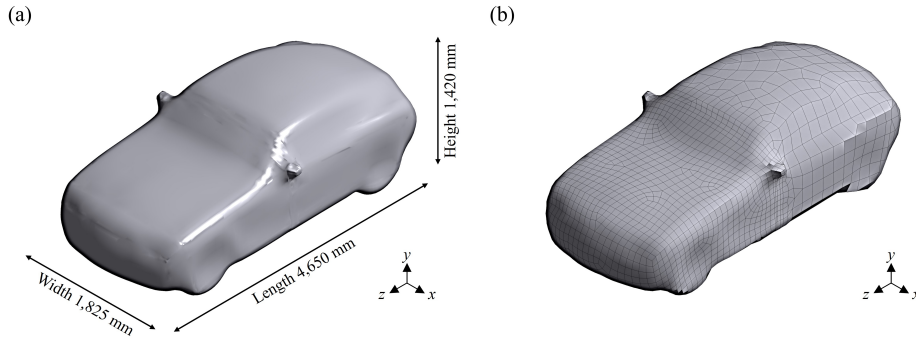


Figure 4: Representation of the vehicle model used in the simulation (a) Vehicle geometry scaled to realistic dimensions. (b) Finite element mesh with refined frontal regions and 3 mm shell thickness for accurate crash prediction.

### 3.2. Data generation and processing

To generate a diverse set of collision scenarios, we apply Latin hypercube sampling (LHS) within the predefined condition ranges: velocities (40–80 km/h), angles (0–45°), offsets (5–100% of vehicle width), and distances (0.3–2 m). A total of 20 distinct  $(v, \theta, o, d)$  combinations were sampled, with 16 used for training and 4 reserved for testing. Each simulation took an average of 32.67 minutes to complete, underscoring the computational cost of dataset generation. Throughout each simulation, the positions of 2,567 nodes are recorded at every time step, yielding a dataset of  $2,567 \times 100 \times 20 = 5.13 \times 10^6$  node instances. Node coordinates are preserved in their original scale to maintain the physical interpretability of displacement magnitudes. Time and collision parameters  $(v, \theta, o, d)$  are normalized to  $[0, 1]$  using min-max scaling. This normalization prevents any single parameter from dominating the input space, ensuring stable training while preserving the physical consistency of the data.

Table 2: Key parameters for the simulation setup.

Category	Description	Value
Geometry	Shell element thickness	3 mm
	Base mesh size	0.3 m
	Number of nodes/elements	2,567 / 2,606
Material	<b>Car: Aluminum Alloy NL</b>	
	Density	2,770 kg/m <sup>3</sup>
	Young's modulus	71 GPa
	Poisson's ratio	0.33
	Yield strength	280 MPa
	Tangent modulus	500 MPa
	<b>Barrier: CONC-35MPA</b>	
	Density	2,314 kg/m <sup>3</sup>
	Compressive strength	35 MPa
	Shear modulus	16.7 GPa
Solid density	2,750 kg/m <sup>3</sup>	
Analysis	Min. time step	1e-9 s
	Time step safety factor	0.9
	Friction coefficient (car-barrier)	0.8 (static), 0.7 (kinetic)

### 3.3. Baseline architectures

We consider two coordinate-based neural networks as baselines: a single MLP and DeepONet. Both models predict spatio-temporal displacements using initial node coordinates, time, and initial collision conditions.

**Single MLP** The single MLP directly maps the inputs  $(\mathbf{x}_{\text{init},i}, t, v, \theta, o, d)$  to the predicted displacement  $\hat{\mathbf{x}}_i \in \mathbb{R}^3$ . This model consists of four fully connected layers with 263 neurons each, resulting in approximately 283k parameters. It serves as a simple baseline for both global motion and local deformation. The overall structure is shown in Figure 5, where each layer uses ReLU activations.

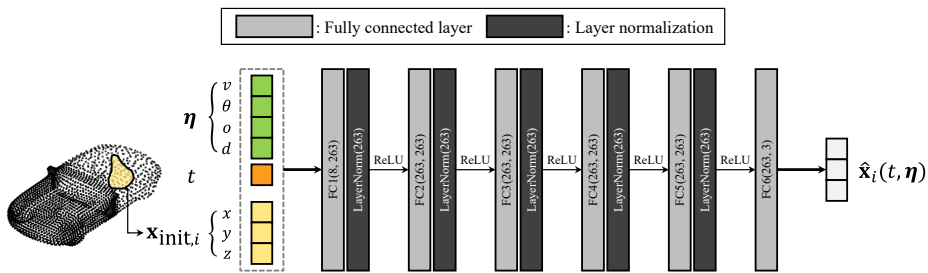


Figure 5: Single MLP architecture. Input: collision conditions  $\eta$ , time  $t$ , and initial node position  $\mathbf{x}_{\text{init},i}$ . The MLP, with four fully connected layers and ReLU activations, predicts the 3D absolute displacement  $\hat{\mathbf{x}}_i$ .

**DeepONet** The DeepONet serves as another baseline, designed to learn a continuous operator that maps collision conditions and time to the displacement field. The branch network encodes  $(v, \theta, o, d)$  into a 32-dimensional latent vector, while the trunk network maps  $(t, \mathbf{x}_{\text{init},i})$

into another 32-dimensional vector. The element-wise dot product of these vectors yields the final displacement  $\hat{\mathbf{x}}_i$ . With approximately 313k parameters, this architecture enables accurate spatio-temporal predictions across diverse collision scenarios. Table 3 provides a summary of trainable parameters for all models, including our proposed model, highlighting differences in model complexity.

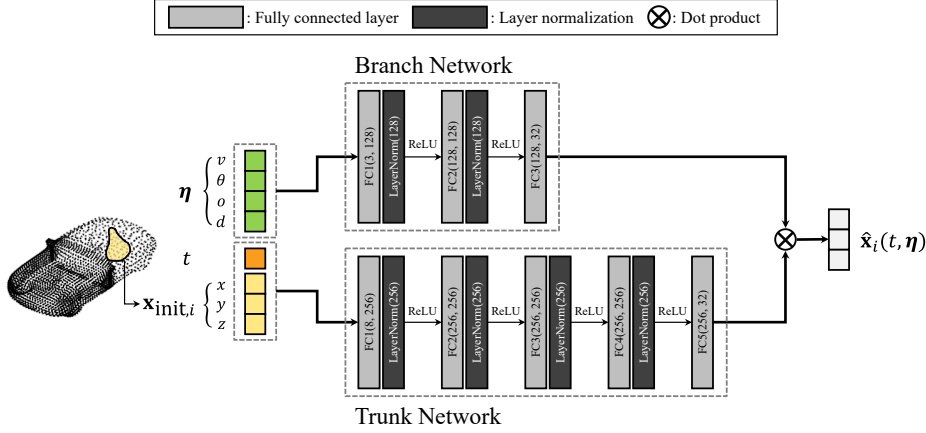


Figure 6: DeepONet architecture. The branch network encodes collision conditions  $\boldsymbol{\eta}$  into a 32-dimensional latent vector. The trunk network maps time  $t$  and initial node position  $\mathbf{x}_{\text{init},i}$  into another 32-dimensional vector. Their element-wise dot product yields the final 3D displacement  $\hat{\mathbf{x}}_i$ .

Table 3: Comparison of trainable parameters across baseline and proposed models

	Single MLP	DeepONet	Proposed
<b>Parameters</b>	283,517	313,472	287,498

To ensure a fair comparison, all models, including the proposed decoupled framework, were trained using the same configuration. All models were trained using the Adam optimizer with an initial learning rate of  $1 \times 10^{-3}$  and a batch size of 1,024, for up to 200 epochs. The mean squared error (MSE) loss was used to optimize node position predictions. All experiments were conducted on an NVIDIA RTX A6000 GPU.

#### 4. Results

This section presents and analyzes the numerical results obtained from the proposed framework across various collision scenarios. The model’s performance is systematically evaluated both within the range of training collision conditions (interpolation) and beyond that range (extrapolation). Additionally, ablation and parametric studies are conducted to quantify the contributions of different model components and to examine the influence of data sampling strategies. These analyses provide a comprehensive evaluation of the framework’s predictive accuracy, computational efficiency, and generalization capabilities.

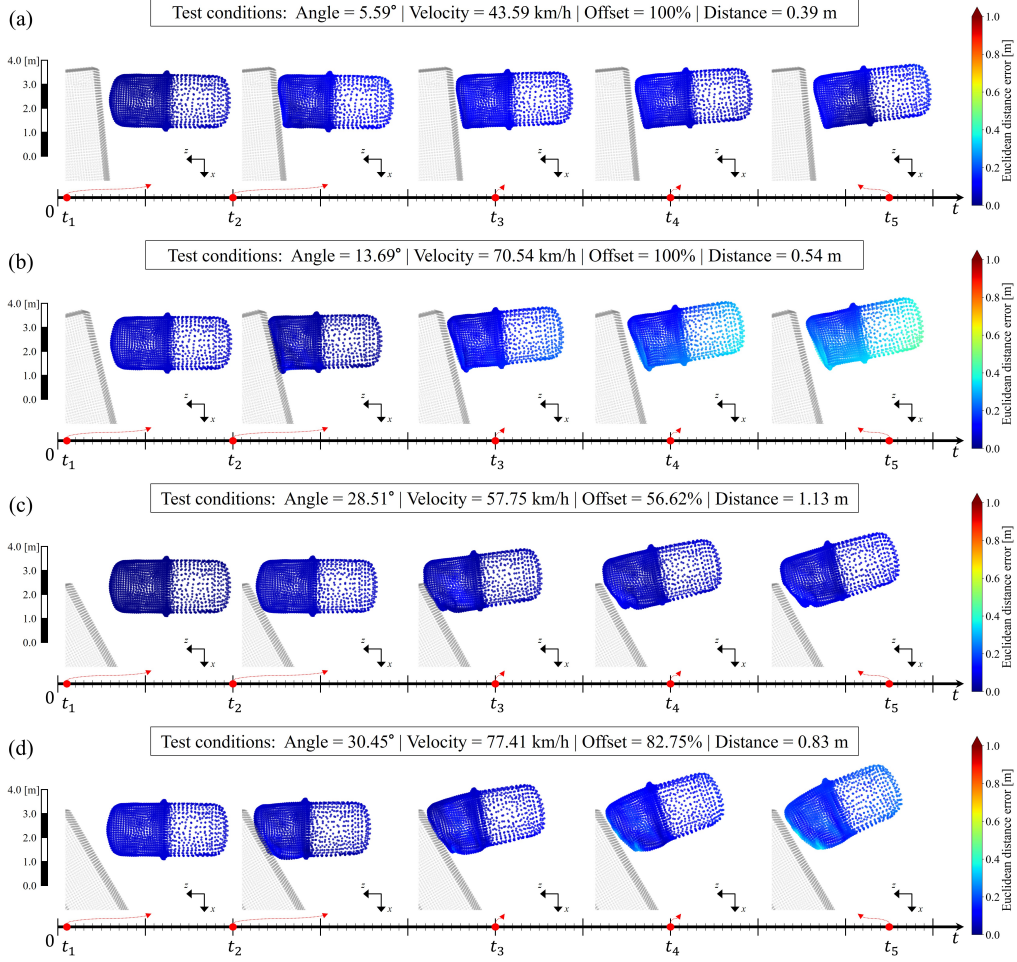


Figure 7: Predicted vehicle displacement for four unseen interpolation scenarios (a)-(d). The model captures both rigid and deformable motion with low error.

#### 4.1. Model performance in interpolation collision scenarios

Figure 7 shows the predicted results for four distinct collision configurations, none of which were included in the training set. Figure 7(a) corresponds to a collision angle of  $5.59^\circ$  and a velocity of 43.59 km/h, with a mean Euclidean distance error below 0.15 across all time steps. This relatively moderate impact scenario illustrates that the network accurately captures both the global yaw motion and the localized structural deformation with minimal discrepancy. Figure 7(b) evaluates the model under more forceful conditions, specified by a  $13.69^\circ$  collision angle and a velocity of 70.54 km/h. Although the overall kinetic energy was higher, the predicted deformation remained well aligned with the ground-truth simulation, with the mean Euclidean distance error across all time steps not exceeding 0.37. The robust performance under these higher-speed conditions indicates that the decoupled prediction of rigid body motion and local deformation accommodates increased momentum transfer without significant degradation

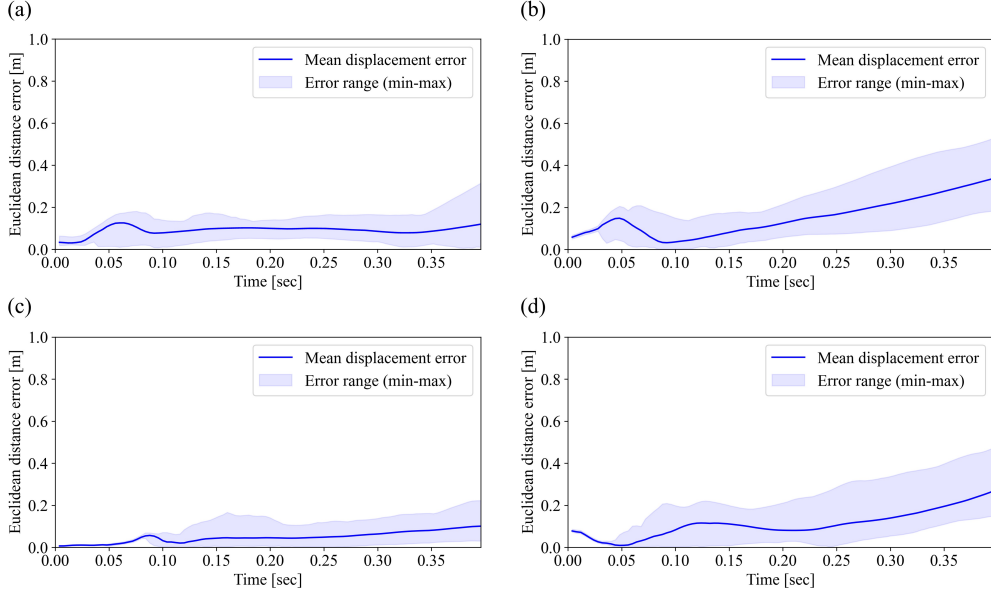


Figure 8: Mean Euclidean distance error over time for interpolation scenarios in Fig. 7, showing stable prediction performance.

of accuracy. Figure 7(c) shows a collision at  $28.51^\circ$  and  $57.75$  km/h, where the geometry of the impact region introduces more complex deformations. Despite the increased angular severity, the mean Euclidean distance error remained below  $0.09$  across all time steps, suggesting that the architecture effectively captures nonlinear deformation patterns arising from oblique impacts. In Fig. 7(d), the collision scenario was characterized by the largest angle of  $30.45^\circ$  and the highest velocity of  $77.41$  km/h among the presented scenarios. Although these extreme conditions induce substantial changes in both inertial loads and local buckling modes, the proposed method consistently maintained a mean Euclidean distance error below  $0.27$  across all time steps. These results confirm that the framework generalizes to untrained angles and speeds within the interpolation domain without requiring explicit modeling of each individual collision scenario. Figure 8 reports the temporal evolution of Euclidean distance error for the same four test conditions shown in Fig. 7. In each subfigure (a)–(d), the error remained stable from the initial moment of impact to the final stage of deformation, indicating that the network efficiently captures both the rapid early-phase collisions and the slower residual motions that occur later. The stability of this time-series behavior implies that decoupling rigid and deformable motion components helps the network maintain accuracy as collisions progress, even under increasingly complex structural responses. The consistency across varying angles and velocities also highlights that the proposed approach successfully learns essential physical factors such as inertial forces, energy dissipation mechanisms, and geometric nonlinearities. These interpolation results collectively demonstrate the robustness of the framework across collision conditions similar to those in the training regime.

Figure 9 presents the training and test loss curves of the proposed model in comparison with a Single MLP and DeepONet. The training loss curves indicate that the proposed framework

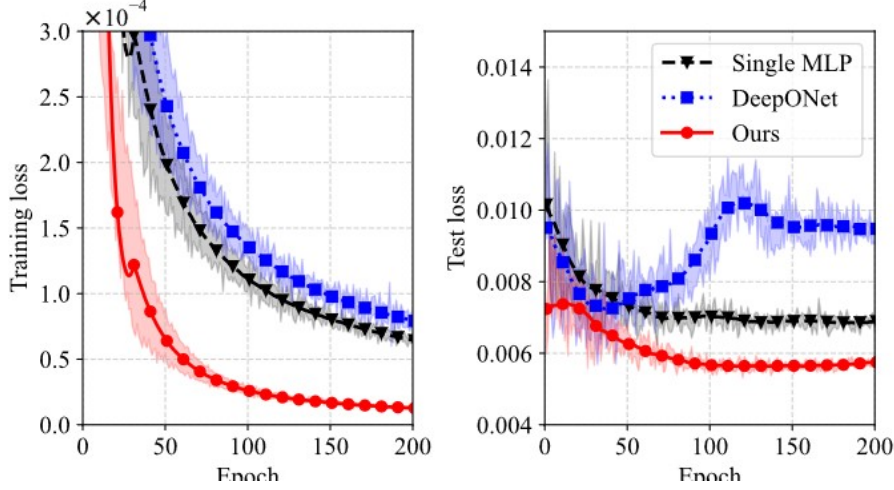


Figure 9: Training and test loss curves for the proposed model, DeepONet, and Single MLP. The proposed model achieves lower loss, indicating better convergence and generalization.

consistently attained lower final losses throughout training. Specifically, the mean training loss over the last 10 epochs was  $0.138 \times 10^{-4}$  for the proposed model, whereas DeepONet and Single MLP yielded mean values of  $0.819 \times 10^{-4}$  and  $0.677 \times 10^{-4}$ , respectively. This corresponds to reductions of 83.15% compared to DeepONet and 79.62% compared to Single MLP, indicating that the decoupled architecture enhances stability and convergence efficiency. A similar trend is evident in the test loss; the proposed model yielded an average test loss of  $0.560 \times 10^{-2}$  over the last 10 epochs, significantly lower than DeepONet ( $0.948 \times 10^{-2}$ ) and Single MLP ( $0.688 \times 10^{-2}$ ). These results correspond to reductions of 40.93% and 18.60%, respectively, indicating improved generalization performance within the interpolation domain. The consistent gap in both training and test loss underscores the benefits of explicitly modeling rigid body motion and local deformation as separate components, resulting in enhanced predictive accuracy and mitigated overfitting.

#### 4.2. Model generalization in extrapolation collision scenarios

To assess the model’s ability to generalize beyond the training domain, we conducted additional evaluations on collision scenarios outside the training dataset. These extrapolation scenarios consist of collision angles, velocities, and offset ratios exceeding the predefined training range (as described in Section 3.2). The framework’s ability to maintain stable performance in unseen conditions is evaluated by comparing its predictions against ground-truth simulation results.

Figure 10 depicts the model’s predictive performance in four extrapolation scenarios. Figure 10(a) shows a scenario with a collision angle of  $50^\circ$ , which exceeds all conditions observed during training. Nevertheless, the model maintains a mean Euclidean distance error below 0.41 across all time steps, suggesting that the learned representation effectively generalizes angular impact dynamics. Figure 10(b) examines an extrapolation scenario at a velocity of 90 km/h. While the model exhibits minor deviations in the rear section of the vehicle, particularly at later time steps ( $t_5$ ) where errors reach up to 0.8, the overall predictive accuracy remains consistent,

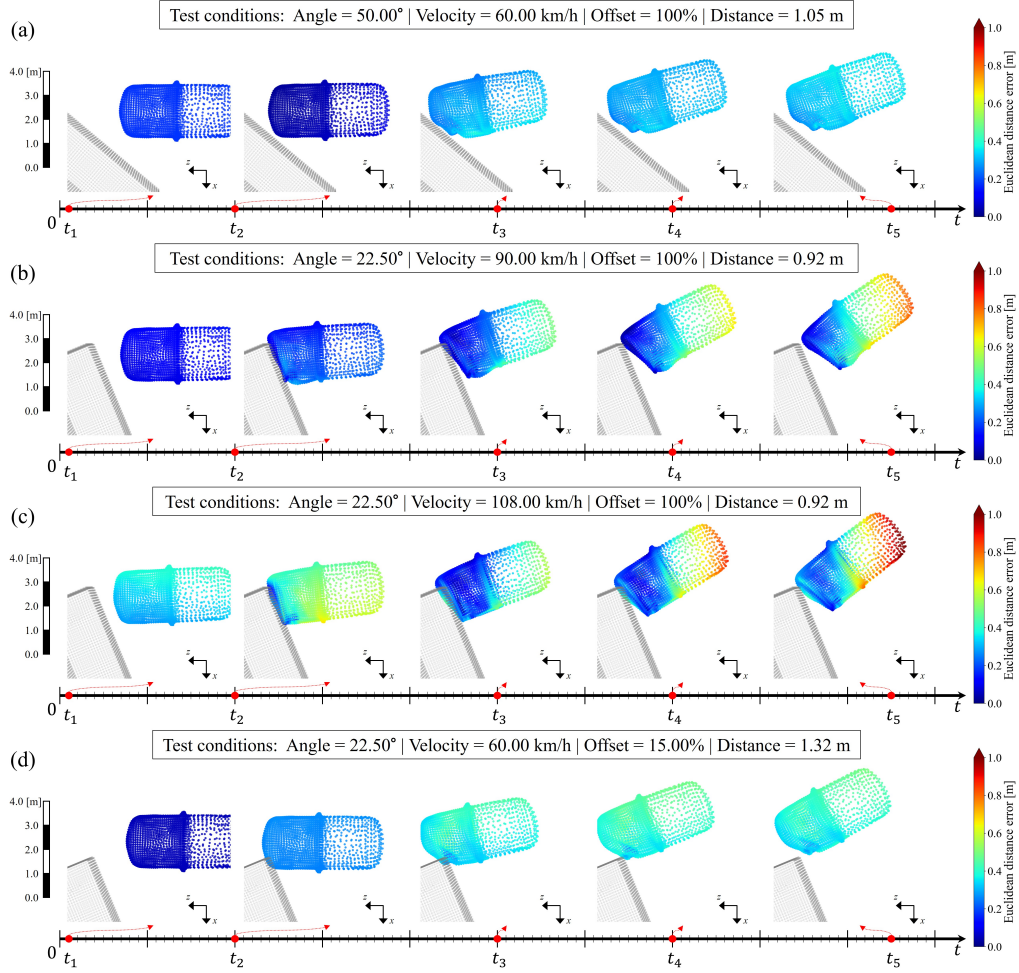


Figure 10: Predicted vehicle displacement for four extrapolation scenarios (a)–(d) outside the training range. The model generalizes well, capturing both rigid and deformable motion.

considering the high-impact severity. Notably, the model continues to accurately capture local deformation patterns despite the extreme collision conditions. In Figure 10(c), an even more extreme velocity extrapolation is evaluated at 108 km/h. As in the previous scenario, slight discrepancies arise in the rear region of the vehicle, with errors remaining below 0.9. However, given the extreme kinetic energy introduced at such high velocities, the model's ability to maintain a stable prediction demonstrates robustness in predicting deformations. Figure 10(d) examines the impact of an extrapolated offset ratio of 15%, where global behavior includes not only yaw motion but also sliding. The model achieves a mean Euclidean distance error below 0.51, demonstrating its ability to predict complex post-impact vehicle motions beyond those observed in training. Importantly, the model successfully captures the emergence of sliding motion, a phenomenon not explicitly present in the training data, further validating its capacity to infer physically consistent global dynamics. These results confirm that the proposed framework goes beyond mere

interpolation and maintains stable predictive performance under unseen impact conditions. The ability to generalize across varying collision parameters demonstrates the effectiveness of the decoupled architecture in learning distinct rigid and deformable motion representations, enhancing its applicability to a broader range of real-world vehicle crash scenarios.

#### 4.3. High-resolution inference in interpolation collision scenarios

To evaluate the model’s capability at increased spatial resolution, we conducted additional inference experiments on simulation data with finer spatial discretization. We obtained the high-resolution ground truth by re-simulating the same interpolation collision scenarios with an element size reduced to one-tenth of its original value. Owing to the constraints imposed by the Courant-Friedrichs-Lewy (CFL) condition, the minimum time step was reduced accordingly to  $1 \times 10^{-9}$ , resulting in a more than tenfold increase in computational cost. This refined discretization allows for more detailed and precise numerical solutions while also inducing slight deviations in the reference displacement field relative to the original ground truth.

Figure 11 depicts the inference results at a higher spatial resolution for the same interpolation scenarios analyzed in Section 4.1. Figures 11(a)–(c) show that the proposed model consistently preserves predictive accuracy even with increased spatial resolution. The overall deformation patterns and rigid body motion closely match the ground truth, indicating that the network effectively generalizes to finer discretizations without necessitating retraining. In Figure 11(d), the predicted displacements show slight deviations relative to the high-resolution reference data. However, this deviation stems not from model failure but from intrinsic differences in the ground-truth simulation. The variation in element size alters the numerical solution, resulting in subtle differences in deformation characteristics. Accordingly, the observed differences are attributed to numerical resolution effects rather than a limitation of the proposed method. These findings confirm that the model reliably infers high-resolution predictions within the interpolation domain, demonstrating its resilience to spatial discretization changes.

#### 4.4. Decoupled rigid and deformable motion analysis

The proposed framework is designed to infer rigid body motion and local deformation as separate components within the latent space. This section examines the results of decoupled inference and evaluates the model’s capability to predict global rigid motion and localized structural deformation independently. In vehicle collision dynamics, rigid body motion and deformation are inherently coupled, posing a challenge in distinguishing them without explicit labels. Shape changes due to deformation are superimposed on the overall translational and rotational motion of the vehicle, complicating time-lapse analysis. Conventional methods rely on multi-body physics simulations or predefined kinematic constraints to isolate these components. In contrast, the proposed architecture learns to separate motion components in the latent space using only absolute displacement data, without explicit supervision for rigid or deformable motion components. This enables the model to predict both global and local vehicle dynamics under diverse impact conditions, enabling real-time collision assessment.

Figure 12 depicts the rigid body motion inference for a specific collision scenario characterized by an impact angle of  $28.51^\circ$  and a velocity of 57.75 km/h. The black solid line represents the rigid motion components (translation and quaternion-based rotation) directly extracted from simulation data, while the red dashed line with circular markers represents the predictions of the *Rigid Net*. The discrepancy between the two is indicated by the blue solid line. The estimation of rigid motion from data follows a geometric approach: the translation component is determined from the center of mass of all node positions at each time step, while the rotation matrix

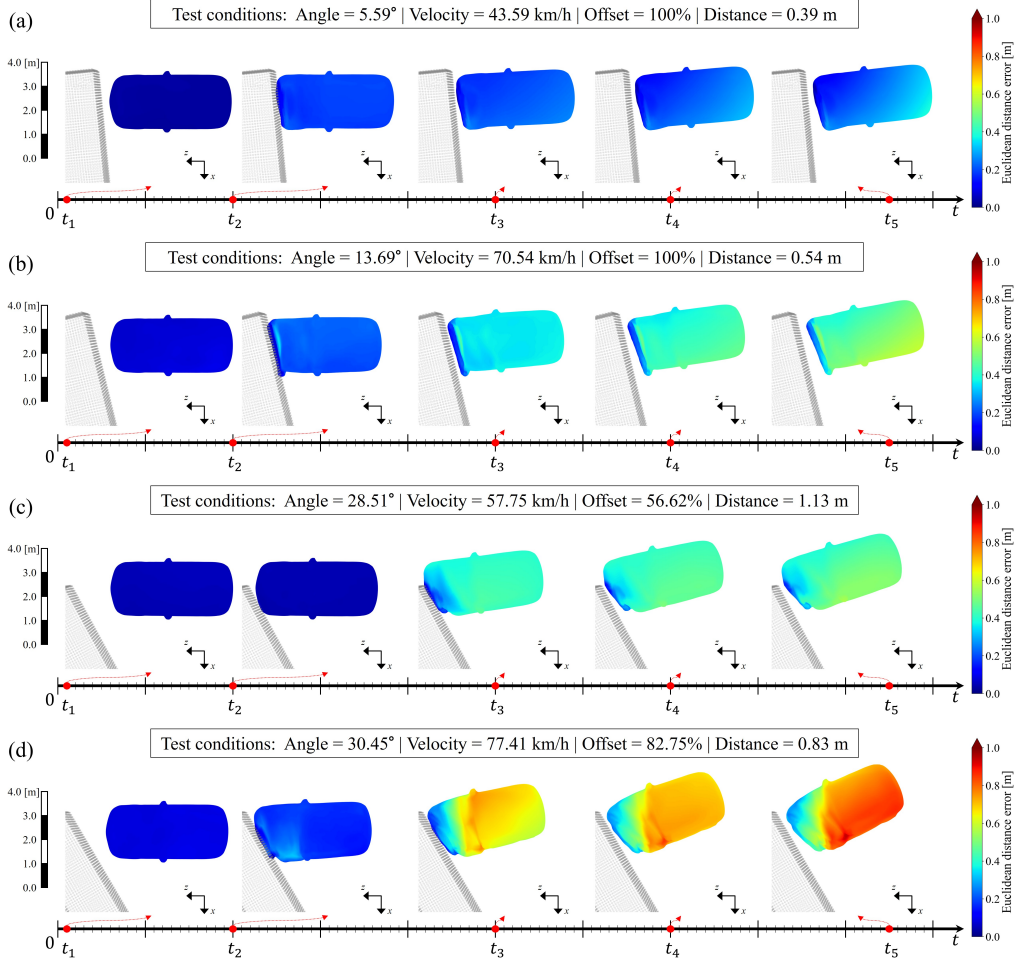


Figure 11: Inference results on high-resolution simulations with finer mesh for unseen interpolation scenarios (a)–(d). The model maintains accuracy across resolutions, capturing fine deformation details.

is obtained using Singular Value Decomposition (SVD). This estimated rigid motion excludes deformation effects and should be considered a reference rather than an absolute ground truth. The close alignment between the *Rigid Net* predictions and the estimated rigid motion suggests that the proposed framework successfully distinguishes rigid motion from deformation within the latent space.

Figure 13 provides additional visualization of the model’s decoupled predictions of rigid and deformable motion. Figure 13(a) shows the predicted motion components at the final time step, including the rigid motion (*Rigid Net*), the deformation field (*Deformation Net*), and their combined output. The model effectively separates rigid and deformable motion components in a physically consistent manner. Figure 13(b) depicts the temporal evolution of rigid body motion, showing that the yaw motion predicted by the *Rigid Net* closely follows expected vehicle dynamics. Figure 13(c) shows the deformation field predicted by the *Deformation Net*, demonstrating

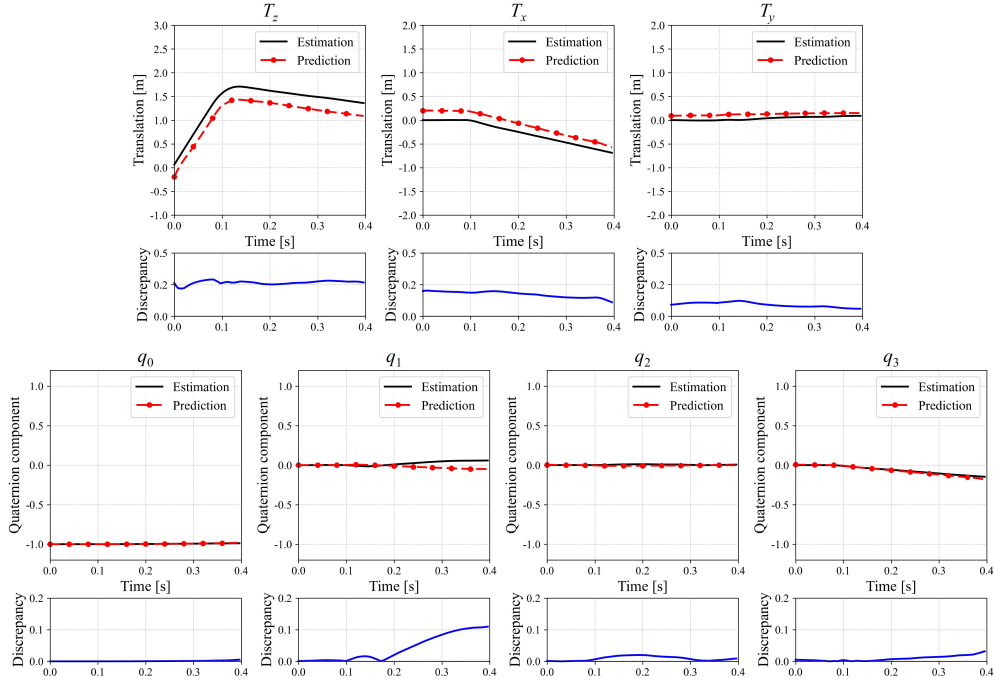


Figure 12: Rigid motion inference for an interpolation scenario (Angle =  $28.51^\circ$ , Velocity = 57.75 km/h, Offset = 56.62%, Distance = 1.13 m). The model closely matches estimated rigid motion, confirming effective separation from deformation.

localized structural changes resulting from impact forces. Finally, Figure 13(d) depicts the total vehicle displacement obtained by combining the rigid and deformation components. These results indicate that the proposed framework successfully decomposes collision dynamics into independent rigid and deformable motion components, despite being trained only on absolute displacement data. Unlike traditional methods that require explicit motion constraints or labeled data for rigid and deformable motion, the model learns this separation in an unsupervised manner through latent space representations. The ability to generalize across different impact scenarios further demonstrates the framework’s robustness in learning a physically meaningful motion decomposition.

## 5. Conclusions

This study proposes a decoupled neural framework for predicting 3D spatio-temporal vehicle collision dynamics. The proposed method implicitly decomposes global rigid body motion and local structural deformation within a latent space without explicit supervision. A quaternion-based *Rigid Net* predicts physically consistent translational and rotational dynamics, while a coordinate-based *Deformation Net* captures complex local structural responses. Quaternion normalization ensures physically valid predictions of rigid body motion.

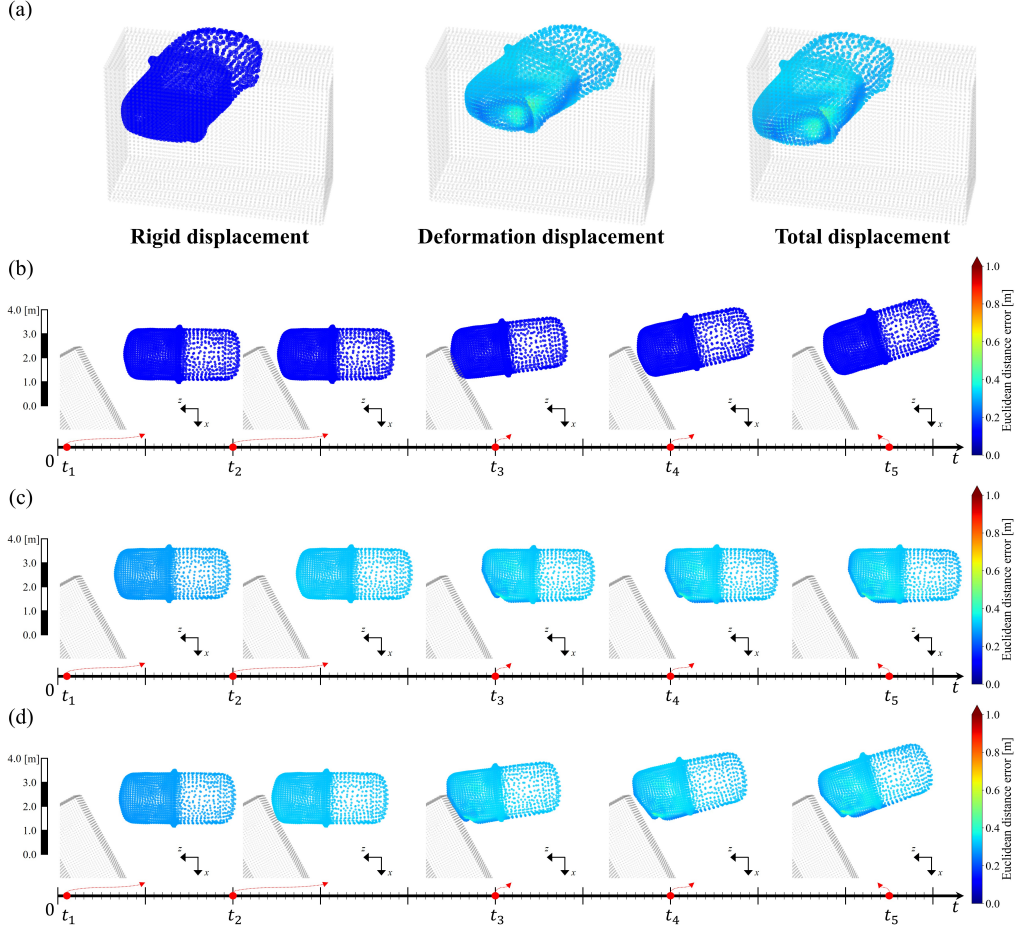


Figure 13: Decoupled rigid and deformable motion predicted by the model. (a) Rigid and deformation components at the final time step. (b) Temporal evolution of rigid motion. (c) Deformation field. (d) Final displacement combining both components.

Experimental results validate the accuracy, efficiency, and generalization capability of the proposed method across diverse collision scenarios. Compared to baseline models, our method achieves up to 83.15% lower prediction errors while reducing computational cost by approximately 83%, enabled by an efficient spatio-temporal sampling strategy. The framework consistently demonstrates accurate performance within interpolation conditions (mean Euclidean distance error below 0.41) and robust generalization to extrapolation scenarios, such as collision velocities up to 108 km/h and angles of  $50^\circ$ , outside the training range. Furthermore, the model exhibits resolution-invariant performance, accurately predicting high-resolution deformation fields from lower-resolution training data, thereby maintaining predictive accuracy without additional computational overhead.

Our key findings demonstrate:

- The proposed decoupled framework effectively separates global rigid body motion and

local structural deformation without explicit supervision, achieving up to 83.15% lower prediction errors compared to baseline models (DeepONet and single MLP).

- The quaternion-based rotation modeling ensures physically consistent predictions, closely matching rigid body dynamics across diverse collision conditions (impact velocities from 40 km/h to 108 km/h and collision angles up to 50°).
- The model demonstrates robust generalization in both interpolation (mean Euclidean distance error below 0.41) and challenging extrapolation scenarios, such as impacts at 108 km/h and collision angles of 50°.
- The spatio-temporal sampling strategy enables efficient learning with only 10% of the training data, reducing training time by approximately 83% while preserving predictive performance.
- The model exhibits resolution-invariant properties, successfully inferring high-resolution deformation fields from lower-resolution training data, reducing reliance on costly high-resolution simulations.

The proposed framework facilitates vehicle safety assessment and design optimization by enabling rapid evaluation of various collision scenarios while reducing computational cost. Future research should extend this approach to vehicle-to-vehicle collisions, incorporate additional physical constraints, such as energy conservation, and investigate integration with reinforcement learning for real-time collision avoidance. Applying transformer architectures may improve the framework's capacity to model complex spatio-temporal patterns in vehicle collision dynamics, possibly enabling higher accuracy and improved generalization.

#### **CRedit authorship contribution statement**

**S. Kim:** Supervision, Conceptualization, Methodology, Software, Validation, Formal analysis, Investigation, Data Curation, Writing – Original Draft, Writing – Review & Editing, Visualization. **M. Seo:** Conceptualization, Writing – Review & Editing. **N. Kang:** Supervision, Funding acquisition.

#### **Declaration of competing interest**

The authors declare that they have no known competing financial interests or personal relationships that could have appeared to influence the work reported in this paper.

#### **Data availability**

Data will be made available on request.

#### **Acknowledgments**

This work was supported by the Ministry of Science and ICT of Korea grant (No. 2022-0-00969, No. 2022-0-00986, and No.GTL24031-000) and the Ministry of Trade, Industry & Energy grant (RS-2024-00410810).

## References

- [1] M. Van Ratingen, A. Williams, L. Anders, A. Seeck, P. Castaing, R. Kolke, G. Adriaenssens, A. Miller, The european new car assessment programme: a historical review, *Chinese journal of traumatology* 19 (02) (2016) 63–69.
- [2] L. Wågström, A. Kling, H. Norin, H. Fagerlind, A methodology for improving structural robustness in frontal car-to-car crash scenarios, *International journal of crashworthiness* 18 (4) (2013) 385–396.
- [3] D. Vangi, Impact severity assessment in vehicle accidents, *International journal of crashworthiness* 19 (6) (2014) 576–587.
- [4] L. Gu, R. Yang, Cae model validation in vehicle safety design, Tech. rep., SAE Technical Paper (2004).
- [5] J. Zhou, H. Peng, J. Lu, Collision model for vehicle motion prediction after light impacts, *Vehicle System Dynamics* 46 (S1) (2008) 3–15.
- [6] D. Yang, T. Gordon, B. Jacobson, M. Jonasson, M. Lidberg, Optimized brake-based control of path lateral deviation for mitigation of secondary collisions, *Proceedings of the Institution of Mechanical Engineers, Part D: Journal of Automobile Engineering* 225 (12) (2011) 1587–1604.
- [7] M. Cao, C. Hu, R. Wang, J. Wang, N. Chen, Compensatory model predictive control for post-impact trajectory tracking via active front steering and differential torque vectoring, *Proceedings of the Institution of Mechanical Engineers, Part D: Journal of Automobile Engineering* 235 (4) (2021) 903–919.
- [8] M. Costas, J. Diaz, L. Romera, S. Hernandez, A multi-objective surrogate-based optimization of the crashworthiness of a hybrid impact absorber, *International Journal of Mechanical Sciences* 88 (2014) 46–54.
- [9] S. Wang, Y. Peng, T. Wang, X. Chen, L. Hou, H. Zhang, The origami inspired optimization design to improve the crashworthiness of a multi-cell thin-walled structure for high speed train, *International Journal of Mechanical Sciences* 159 (2019) 345–358.
- [10] J. Fang, G. Sun, N. Qiu, N. H. Kim, Q. Li, On design optimization for structural crashworthiness and its state of the art, *Structural and Multidisciplinary Optimization* 55 (2017) 1091–1119.
- [11] A. Pifko, R. Winter, Theory and application of finite element analysis to structural crash simulation, in: *Computational Methods in Nonlinear Structural and Solid Mechanics*, Elsevier, 1981, pp. 277–285.
- [12] N. Formosa, M. Quddus, S. Ison, M. Abdel-Aty, J. Yuan, Predicting real-time traffic conflicts using deep learning, *Accident Analysis & Prevention* 136 (2020) 105429.
- [13] L. Paparusso, S. Melzi, F. Braghin, Real-time forecasting of driver-vehicle dynamics on 3d roads: A deep-learning framework leveraging bayesian optimisation, *Transportation research part C: emerging technologies* 156 (2023) 104329.

- [14] V. Katariya, M. Baharani, N. Morris, O. Shoghli, H. Tabkhi, Deeptrack: Lightweight deep learning for vehicle trajectory prediction in highways, *IEEE Transactions on Intelligent Transportation Systems* 23 (10) (2022) 18927–18936.
- [15] J. Kim, J. Park, N. Kim, Y. Yu, K. Chang, C.-S. Woo, S. Yang, N. Kang, Physics-constrained graph neural networks for spatio-temporal prediction of drop impact on oled display panels, *Expert Systems with Applications* (2025) 126907.
- [16] S. Yang, R. Vinuesa, N. Kang, Towards robust spatio-temporal auto-regressive prediction: Adams-bashforth time integration with adaptive multi-step rollout, *arXiv preprint arXiv:2412.05657* (2024).
- [17] S. Kumawat, M. Verma, Y. Nakashima, S. Raman, Depthwise spatio-temporal stft convolutional neural networks for human action recognition, *IEEE Transactions on Pattern Analysis and Machine Intelligence* 44 (9) (2021) 4839–4851.
- [18] P. W. Battaglia, J. B. Hamrick, V. Bapst, A. Sanchez-Gonzalez, V. Zambaldi, M. Malinowski, A. Tacchetti, D. Raposo, A. Santoro, R. Faulkner, et al., Relational inductive biases, deep learning, and graph networks, *arXiv preprint arXiv:1806.01261* (2018).
- [19] A. Sanchez-Gonzalez, J. Godwin, T. Pfaff, R. Ying, J. Leskovec, P. Battaglia, Learning to simulate complex physics with graph networks, in: *International conference on machine learning*, PMLR, 2020, pp. 8459–8468.
- [20] L. Lu, P. Jin, G. Pang, Z. Zhang, G. E. Karniadakis, Learning nonlinear operators via deeponet based on the universal approximation theorem of operators, *Nature machine intelligence* 3 (3) (2021) 218–229.
- [21] D. Rempe, S. Sridhar, H. Wang, L. Guibas, Learning generalizable final-state dynamics of 3d rigid objects, in: *Proceedings of the IEEE/CVF Conference on Computer Vision and Pattern Recognition Workshops*, 2019, pp. 17–20.
- [22] D. Rempe, S. Sridhar, H. Wang, L. Guibas, Predicting the physical dynamics of unseen 3d objects, in: *Proceedings of the IEEE/CVF Winter Conference on Applications of Computer Vision*, 2020, pp. 2834–2843.
- [23] J. Zhou, H. Peng, J. Lu, Collision model for vehicle motion prediction after light impacts, *Vehicle System Dynamics* 46 (S1) (2008) 3–15.
- [24] H. Minamoto, S. Takezono, Two-dimensional motion of vehicles damaged due to collision, *Vehicle System Dynamics* 34 (4) (2000) 229–248.
- [25] X. Zhang, Z. Hu, X. Du, Probabilistic inverse simulation and its application in vehicle accident reconstruction, *Journal of Mechanical Design* 135 (12) (2013) 121006.
- [26] Z. Wen, Y. Li, H. Wang, Y. Peng, Data-driven spatiotemporal modeling for structural dynamics on irregular domains by stochastic dependency neural estimation, *Computer Methods in Applied Mechanics and Engineering* 404 (2023) 115831.
- [27] E. Sakaridis, N. Karathanasopoulos, D. Mohr, Machine-learning based prediction of crash response of tubular structures, *International Journal of Impact Engineering* 166 (2022) 104240.

- [28] S. Shin, A.-h. Jin, S. Yoo, S. Lee, C. Kim, S. Heo, N. Kang, Wheel impact test by deep learning: prediction of location and magnitude of maximum stress, *Structural and Multi-disciplinary Optimization* 66 (1) (2023) 24.
- [29] E. G. Hemingway, O. M. O'Reilly, Perspectives on euler angle singularities, gimbal lock, and the orthogonality of applied forces and applied moments, *Multibody system dynamics* 44 (2018) 31–56.
- [30] J. Diebel, et al., Representing attitude: Euler angles, unit quaternions, and rotation vectors, *Matrix* 58 (15-16) (2006) 1–35.
- [31] D. M. Henderson, Euler angles, quaternions, and transformation matrices for space shuttle analysis, Tech. rep. (1977).
- [32] R. Mukundan, R. Mukundan, Quaternions, *Advanced Methods in Computer Graphics: With examples in OpenGL* (2012) 77–112.
- [33] D. P. Kingma, J. Ba, Adam: A method for stochastic optimization, In *3rd international conference on learning representations* (2015).
- [34] A. X. Chang, T. Funkhouser, L. Guibas, P. Hanrahan, Q. Huang, Z. Li, S. Savarese, M. Savva, S. Song, H. Su, et al., Shapenet: An information-rich 3d model repository, *arXiv preprint arXiv:1512.03012* (2015).
- [35] U. S. D. of Defense, *Military Handbook: Metallic Materials and Elements for Aerospace Vehicle Structures*, Vol. 1, US Department of Defense, 1990.
- [36] W. Riedel, K. Thoma, S. Hiermaier, E. Schmolinske, Penetration of reinforced concrete by beta-b-500 numerical analysis using a new macroscopic concrete model for hydrocodes, in: *Proceedings of the 9th International Symposium on the Effects of Munitions with Structures*, Vol. 315, Berlin-Strausberg Germany, 1999.
- [37] W. Riedel, *Beton unter dynamischen lasten* (2004).
- [38] W. Riedel, N. Kawai, K.-i. Kondo, Numerical assessment for impact strength measurements in concrete materials, *International Journal of Impact Engineering* 36 (2) (2009) 283–293.
- [39] B. Rabbat, H. Russell, Friction coefficient of steel on concrete or grout, *Journal of Structural Engineering* 111 (3) (1985) 505–515.